Structure

Article

Fungal kinesin-8 motors dimerize by folding their proximal tail domain into a compact helical bundle

Graphical abstract

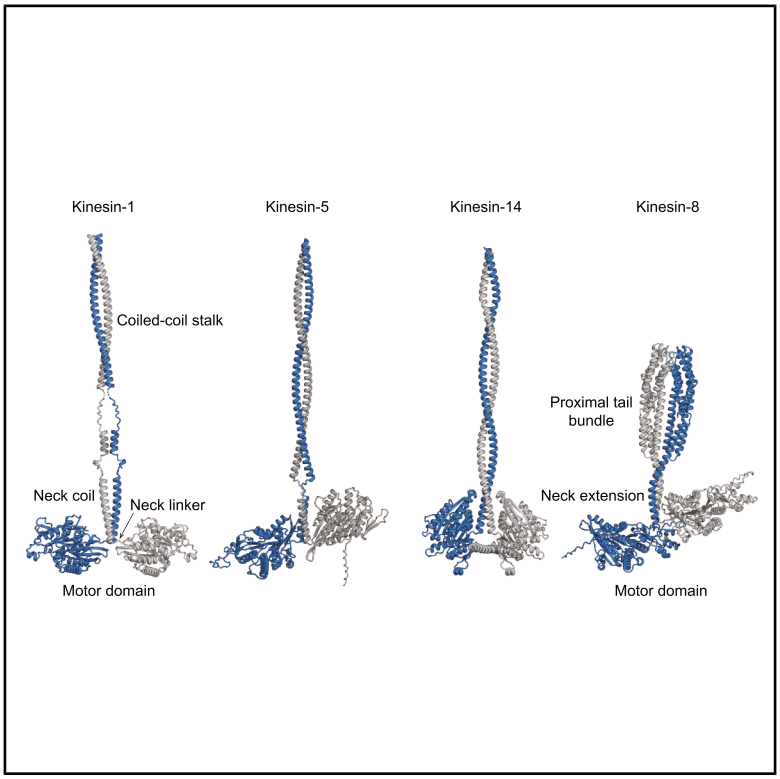

Authors

Daria Trofimova, Caitlin Doubleday, Byron Hunter, ..., Eric Wen, Kim Munro, John S. Allingham

Correspondence

allinghj@queensu.ca

In brief

Trofimova et al. reveal that fungal kinesin-8 motors dimerize via a compact four-helix tail bundle, rather than a canonical coiled coil. A flexible, non-dimerizing neck extension links this bundle to the motor domains, suggesting a modular architecture that may support kinesin-8's unique ability to couple motility with microtubule depolymerization.

Highlights

- The architecture of kinesin-8 tails differs from the coiled-coil in other kinesins
- Their proximal tail forms a compact helix bundle that dimerizes
- A flexible hinge separates the upper and lower lobules of the bundle
- The adjacent neck extension is flexible and does not mediate dimerization

Trofimova et al., 2025, Structure *33*, 1–11
December 4, 2025
https://doi.org/10.1016/j.str.2025.08.011

CellPress

Please cite this article in press as: Trofimova et al., Fungal kinesin-8 motors dimerize by folding their proximal tail domain into a compact helical bundle, Structure (2025), https://doi.org/10.1016/j.str.2025.08.011

Structure

CellPress

Article

Fungal kinesin-8 motors dimerize by folding their proximal tail domain into a compact helical bundle

Daria Trofimova,[1] Caitlin Doubleday,[1] Byron Hunter,[1] Jesus Danilo Serrano Arevalo,[1] Emma Davison,[1] Eric Wen,[1] Kim Munro,[1] and John S. Allingham[1,2,*]

[1]Department of Biomedical and Molecular Sciences, Queen's University, Kingston, ON K7L 3N6, Canada

[2]Lead contact

*Correspondence: allinghj@queensu.ca

https://doi.org/10.1016/j.str.2025.08.011

SUMMARY

Kinesin-8 motors regulate kinetochore-microtubule dynamics and control spindle length and positioning. Certain isoforms achieve this by traversing microtubules, accumulating at plus-ends, and depolymerizing terminal αβ-tubulin subunits. While the kinesin-8 motor domain is well characterized, the tail domain regions are less understood. Using the *Candida albicans* Kip3 protein as a model for fungal kinesin-8, we present an X-ray crystal structure and hydrodynamic analysis of its motor-proximal tail segment, revealing its role in motor dimerization. This segment forms a compact, 92 Å-long four-helix bundle, rather than an elongated coiled-coil stalk seen in most kinesins. The bundle is stabilized primarily by interactions between helices one and three, with additional support from helices two and four. A flexible hinge bisects the bundle into two lobules, imparting mechanical pliability and asymmetric exterior surfaces. These unique features may facilitate interactions with regulatory elements or contribute to the functional versatility of kinesin-8 motors.

INTRODUCTION

Motor proteins of the kinesin, dynein, and myosin families generate the mechanical forces essential for a wide range of cellular processes, including cell division, intracellular transport, and motility. Despite operating along distinct cytoskeletal tracks—kinesins and dyneins on microtubules and myosins on actin filaments—these motors share common architectural features: (1) a catalytic motor domain that couples ATP turnover to conformational changes, (2) a neck or neck-linker region that amplifies motor domain movements, and (3) a tail domain that mediates interactions with cargo or the cytoskeleton.[1]

A further shared feature of these motors is the presence of oligomerization domains, typically within the tail region. In muscle and certain non-muscle myosins, dimerization is facilitated by extended coiled-coil regions in their tail that can span up to 500 Å.[2,3] This architecture positions the motor domains to engage actin filaments, enabling muscle contraction or hand-over-hand motility. Similarly, most kinesins dimerize through a long coiled-coil stalk linking the motor domains to the tail.[4] This configuration supports processive motion of individual kinesins or kinesin teams along microtubules.[5,6] Dyneins also rely on tail-mediated dimerization, but their activity is further regulated by accessory subunits that modulate motility and promote minus-end-directed cargo transport.[7–10]

Initial insights into kinesin oligomerization emerged from structural studies of kinesin-14 (Ncd), where Sablin et al. described a 43-residue coiled-coil tethering two motor domains in close proximity.[11] Later studies by Kozielski et al. on kinesin-1 and Nithianantham et al. on kinesin-5 revealed dimeric and tetrameric tail assemblies, including four-helix bundles spanning up to ~170 residues.[12,13] More recently, cryo-electron microscopy and AlphaFold predictions have captured kinesin-1 dimers in autoinhibited and light chain-bound states, illuminating how tail structures regulate activity.[14] However, the oligomeric architectures of many kinesin families remain poorly characterized, particularly for the kinesin-8 family.

Kinesin-8s are distinguished by their bimodal functionality, switching between processive motility and microtubule plus-end depolymerization.[15–19] This dual behavior may be enabled by a unique mode of oligomerization, but no X-ray crystallographic or cryo-EM structures of the non-motor domains have been elucidated for a kinesin-8. Functional studies on the *Saccharomyces cerevisiae* kinesin-8 (*Sc*Kip3) suggest that its proximal and distal tail segments independently regulate its mitotic functions.[20] The proximal tail restricts *Sc*Kip3's microtubule-depolymerization activity to astral microtubules near the bud neck, contributing to spindle alignment, while the distal tail prevents *Sc*Kip3 from depolymerizing microtubules at the spindle midzone during anaphase, preserving spindle integrity until chromosome segregation concludes.[21] The structures of these tail segments, and the mechanisms underlying their ability to spatially restrict the activities of *Sc*Kip3, remain unknown.

Please cite this article in press as: Trofimova et al., Fungal kinesin-8 motors dimerize by folding their proximal tail domain into a compact helical bundle, Structure (2025), https://doi.org/10.1016/j.str.2025.08.011

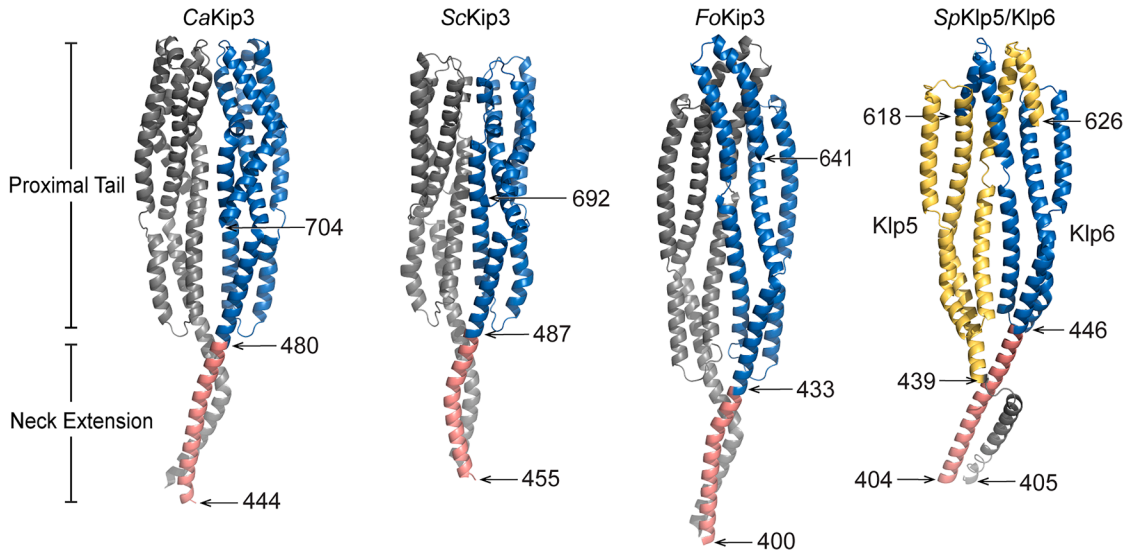

Figure 1. AlphaFold3-predicted dimer structures of the neck extension and proximal tail domain of fungal kinesin-8 motors

Dimeric structural models of *Candida albicans* Kip3 (*Ca*Kip3), *Saccharomyces cerevisiae* Kip3 (*Sc*Kip3), *Fusarium oxysporum* Kip3 (*Fo*Kip3), and *Schizosaccharomyces pombe* Klp5/Klp6 heterodimer (*Sp*Klp5/6) were generated using AlphaFold3. Two Mg^{2+} ions and two ATP ligands were included in all predictions to fill the nucleotide pocket of their motor domains. The figures show only the neck extension and proximal tail regions of these dimer models. The neck extension is colored pink and proximal tail is colored blue for one of the subunits. The other subunit is colored gray. In the *Sp*Klp5/Klp6 heterodimer model, Klp5 is colored yellow and gray and Klp6 is colored blue and pink. The amino acid numbers for the domain boundaries are shown next to arrows. Cartoon representations were generated using PyMOL.[22] Dimeric structural models of the full proteins are presented in Figure S3.

To address the gap in structural knowledge, we used AlphaFold3 to predict full-length homodimeric structures of kinesin-8 proteins. The models indicate that fungal kinesin-8s—including those from *Saccharomyces cerevisiae*, *Schizosaccharomyces pombe*, *Candida albicans*, and *Fusarium oxysporum*—dimerize through a compact four-helix bundle formed by their proximal tail region (Figure 1). To experimentally test these predictions, we focused on *Candida albicans* Kip3 (*Ca*Kip3), which has served as a model for understanding how kinesin-8 motor domains alternate between motility and depolymerization based on microtubule protofilament geometry.[23] We analyzed a series of *Ca*Kip3 truncations using a combination of X-ray crystallography, analytical ultracentrifugation, and size-exclusion chromatography coupled with multi-angle light scattering. Our data confirm that the *Ca*Kip3 proximal tail forms a compact four-helix bundle consistent with AlphaFold3 models. This structure mediates motor dimerization, whereas the immediately upstream α-helical segment does not—in contrast to dimerization strategies observed in kinesin-1, -5, and -14.

RESULTS

The proximal tail forms the dimerization domain of kinesin-8

Kinesin tails frequently contain extended α-helical regions immediately before or after their motor domain that mediate dimerization through coiled-coil interactions (Figure S1A).[24] These coiled coils are typically characterized by heptad repeats, where hydrophobic amino acids, such as leucine or isoleucine occupy positions 1 and 4, and charged residues occur at position 5 and 7.[25] In fungal kinesin-8s, however, this pattern is both shorter (30–40 residues) and imperfect (Figures S1A and S2),[26–28] raising the question about how these motors achieve stable dimerization. To investigate this, we used AlphaFold3 to model the dimeric structures of four fungal and three metazoan kinesin-8 proteins using protein sequences obtained from UniProt.[29] While the global folding of full-length proteins was predicted with low confidence (pLDDT 50–70), the motor domain and proximal tail regions were modeled with high confidence based on both pLDDT (>70) and predicted aligned error (PAE) scores (Figure S3).

Unexpectedly, AlphaFold3 predicts that the region between the motor domain and proximal tail, here termed the "neck extension", adopts a configuration of parallel, non-intertwined helices rather than forming a canonical coiled coil as seen in other kinesins (Figures 1 and S1B). In fungal kinesin-8s, these helices transition into a four-helix bundle that assembles a symmetric proximal tail homodimer, featuring conserved helical lengths, conformations, and intersubunit contacts across species. A similar bundle is also predicted in the proximal tails of metazoan kinesin-8s, including *Drosophila melanogaster* Klp67A and human Kif18A and Kif19 (Figure S3). However, their bundles differ in topology and exhibit greater helix continuity compared to their fungal counterparts (Figure S4). The **distal tail**, which follows the proximal tail, is consistently predicted to be **unstructured** across all species examined (Figure S3).

To experimentally test these predictions, we attempted to express full-length *Candida albicans* Kip3 (*Ca*Kip3) in both *E. coli* and insect cells but found that expression was consistently low and the protein poorly soluble. We therefore designed and expressed six truncated *Ca*Kip3 constructs in *E. coli* BL21 (DE3) cells, guided by the AlphaFold3 structural model (Figure 2). Three constructs contained the motor domain (MD), neck linker (NL), and variable regions extending into the tail: **MD-NL** includes the MD and NL (residues 2–436), **MD-NE** includes the MD, NL,

Please cite this article in press as: Trofimova et al., Fungal kinesin-8 motors dimerize by folding their proximal tail domain into a compact helical bundle, Structure (2025), https://doi.org/10.1016/j.str.2025.08.011

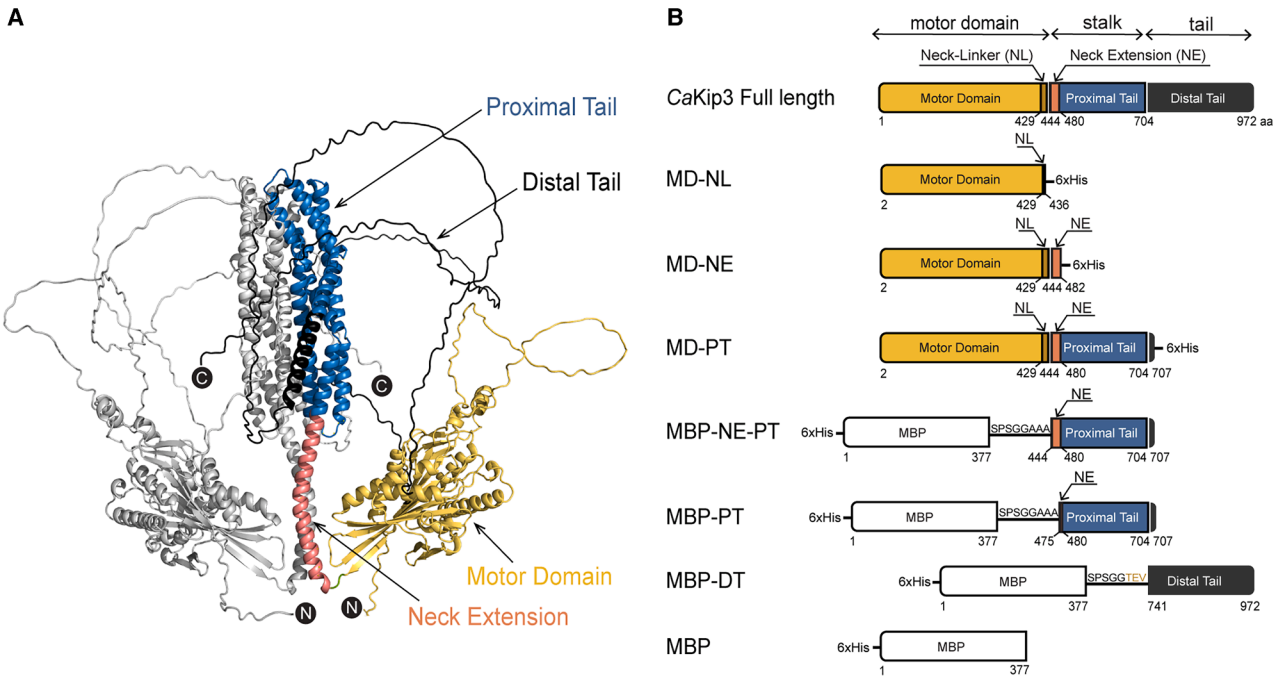

Figure 2. AlphaFold3 model of the full *Ca*Kip3 dimer and domain-specific construct diagrams

(A) Predicted structure of the full *Ca*Kip3 dimer. One monomer is shown in light gray, while the second monomer is color-coded based on the domain map in (B). (B) Domain schematic of *Ca*Kip3, illustrating the motor domain (MD, yellow), neck linker (NL, brown), neck extension (NE, pink), proximal tail domain (PT, blue), and distal tail domain (DT, black). The truncated constructs used in structural and functional studies are depicted below with their respective domain boundaries. Placement of affinity chromatography purification tags (6xHis), maltose-binding protein (MBP) tags, and linkers used for the constructs are shown.

and neck extension (NE) (residues 2–482), and MD-PT includes the MD, NL, NE, and proximal tail (PT) (residues 2–707). These constructs carried C-terminal 6×His-tags and were purified via Ni-NTA affinity chromatography. The remaining constructs focused on the tail segments and were fused to an N-terminal 6×His-tag and a maltose-binding protein (MBP) to enhance solubility: NE-PT (residues 444–707), PT (residues 475–707), and DT (distal tail) (residues 741–972). SDS-PAGE analysis of the purified proteins is shown in Figure S5A.

To determine the oligomeric states of each construct, we employed size-exclusion chromatography with multiangle light scattering (SEC-MALS) and analytical ultracentrifugation (AUC). These methods showed that MD-NL, MD-NE, MBP-DT, along with the MBP-only control, have molecular masses consistent with the calculated mass of their monomeric forms (Figures 3A, 3B, 3F, 3G, S5B, S5C, S5F, and S6). In contrast, the MBP-NE-PT, MBP-PT, and MD-PT constructs exhibited molecular masses approximately double their monomeric forms (Figures 3C, 3D, 3E, 3G, S5D, and S5E). Therefore, the region corresponding to the neck extension that was predicted to form a short coiled coil (residues 444–471) did not induce dimerization of the motor domain (MD-NE), while inclusion of the proximal tail did (MD-PT) (Figure 3E). Also, the proximal tail region alone (MBP-PT) was sufficient to form stable dimers, while the distal tail region (MBP-DT) did not. These results indicate that the proximal tail is the principal structural determinant for *Ca*Kip3 dimerization not the neck extension or the distal tail.

While AUC clearly distinguished monomeric and dimeric species, SEC-MALS detected minor amounts of higher molecular weight species in the MD-NL, MD-NE, and MBP samples (Figures 3A, 3B, and S6). These were likely either impurities, which we also observe by SDS-PAGE (Figure S5A), or transient aggregates, as their masses do not correspond to protein dimers (Figure 3G). It is also important to note MBP does not promote oligomerization of fusion proteins,[30] so the dimer-sized masses of MBP-NE-PT and MBP-PT is not a consequence of their added MBP.

Molecular architecture of the CaKip3 proximal tail

To determine the structure of the *Ca*Kip3 proximal tail, we subjected the MBP-tagged NE-PT and PT constructs to sparse-matrix crystallization screening using sitting-drop vapor diffusion. Crystals formed within one week for both constructs, but only the MBP-PT crystals diffracted X-rays to sufficient resolution for structure determination. Synchrotron diffraction data collected from single crystals enabled structure solution at 2.5 Å resolution by molecular replacement (MR), using one subunit from the AlphaFold3-predicted *Ca*Kip3 PT dimer as the search model. The best MR solution revealed eight PT subunits (A-H) in the asymmetric unit. Each subunit adopts a compact four-helix bundle architecture (Figure 4A), closely resembling the AlphaFold3 prediction (root-mean-square deviation [RMSD] = 0.989 Å; Figure S7), but with no structural similarity to any protein in the Protein DataBank (PDB). As predicted by AlphaFold3, two PT subunits form a parallel dimer through tight packing of helices 1 and 3, aligning their N termini in the same direction (Figures 4B and 4C). This configuration would juxtapose the two motor domains in a dimeric motor complex. Within the asymmetric unit,

Please cite this article in press as: Trofimova et al., Fungal kinesin-8 motors dimerize by folding their proximal tail domain into a compact helical bundle, Structure (2025), https://doi.org/10.1016/j.str.2025.08.011

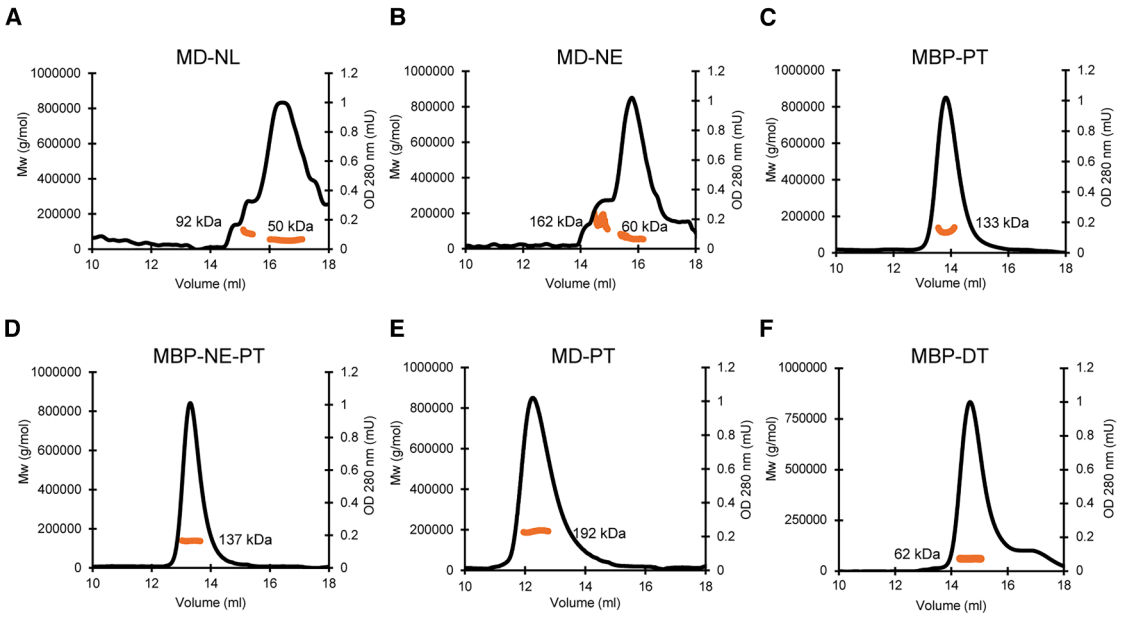

G

	MD-NL	MD-NE	MBP-PT	MBP-NE-PT	MD-PT	MBP-DT	MBP
Theoretical Mw, kDa	49	54.7	69.5	73.1	80	68	42
SEC-MALS, kDa	50	60	133	137	192	62	48
AUC, kDa	47.6	54.2	133	145	ND	ND	41.6
Oligomeric state	monomer	monomer	dimer	dimer	dimer	monomer	monomer

Figure 3. SEC-MALS analysis of the *Ca*Kip3 constructs

(A–F) Size exclusion chromatography-multi-angle light scattering (SEC-MALS) analysis of 20 μM solutions of the following *Ca*Kip3 constructs: (A) motor domain-neck linker (MD-NL), (B) motor domain-neck extension (MD-NE), (C) MBP-proximal tail domain (MBP-PT), (D) MBP-neck extension-proximal tail domain (MBP-NE-PT), (E) motor domain-proximal tail (MD-PT), and (F) MBP-distal tail domain (MBP-DT). Constructs were analyzed in a buffer containing 20 mM HEPES, 1 mM $MgCl_2$ 0.2 mM ATP, 150 mM NaCl, 1 mM DTT, pH 7.0.

(G) Summary of theoretical and experimentally determined molecular weights (Mw) for all constructs using SEC-MALS and analytical ultracentrifugation (AUC).

four such dimers (AB, CD, EF, and GH) were arranged in two anti-parallel planes, with EF and GH rotated ~60° relative to AB and CD (Figure 4D).

Unexpectedly, no electron density corresponding to the N-terminal MBP tag was observed in the final structure, nor was there sufficient space within the lattice to accommodate MBP. To investigate this, we analyzed the protein content of the crystals. Although SDS-PAGE analysis of dissolved crystals did not resolve distinct bands (Figure S8A), prolonged incubation of the MBP-PT fusion protein in the crystallization buffer at room temperature led to the appearance of four major proteolytic fragments (52, 42, 27, and 18 kDa) (Figure S8C). Western blotting with an anti-His antibody detected the full 69.5 kDa protein and the 52 and 42 kDa fragments, but not the 27 or 18 kDa fragments (Figure S8D), suggesting that the latter lacked the MBP and His-tag. These findings indicate that proteolysis occurred near the region linking MBP to the proximal tail, liberating a protease-resistant proximal tail domain. The 27 kDa fragment matches size of the crystallized domain, suggesting that cleavage yielded a structurally stable tail segment that was competent for crystal formation (Figure S8B).

The dimerization interface

To characterize the *Ca*Kip3 PT dimer interface, we analyzed the crystallographic dimers using PDBePISA.[31] Dimer formation buried up to **2,803 Å^2** of each subunit's total surface area (**15,041 Å^2**), consistent with a substantial and stable interface. Electrostatic surface mapping of the *Ca*Kip3 PT monomer identified two prominent non-polar patches oriented along the vertical axis (Figures 5A and 5B). One of these patches corresponds to the dimer interface, while the other aligns with the inter-dimer crystal contact site, suggesting that hydrophobic interactions dominate both dimer formation and lattice packing.

The **2.5 Å** electron density maps allowed confident modeling of most side chains within the proximal tail (Figure 5C), enabling detailed analysis of inter-subunit contacts. Using the Protein Contacts Atlas,[32] we identified **102** interfacial contacts, with helices 1b and 3a forming the majority (Figure 5D). Notably, helix 3a engages in extensive hydrophobic and polar contacts with its counterpart (3a′) and with helix 1b′ from the opposite subunit. Several of these contacts involve residues conserved in fungal kinesin-8 homologs, including *S. cerevisiae* and *S. pombe* (green and blue dots, Figure S2). Among these, six polar

Please cite this article in press as: Trofimova et al., Fungal kinesin-8 motors dimerize by folding their proximal tail domain into a compact helical bundle, Structure (2025), https://doi.org/10.1016/j.str.2025.08.011

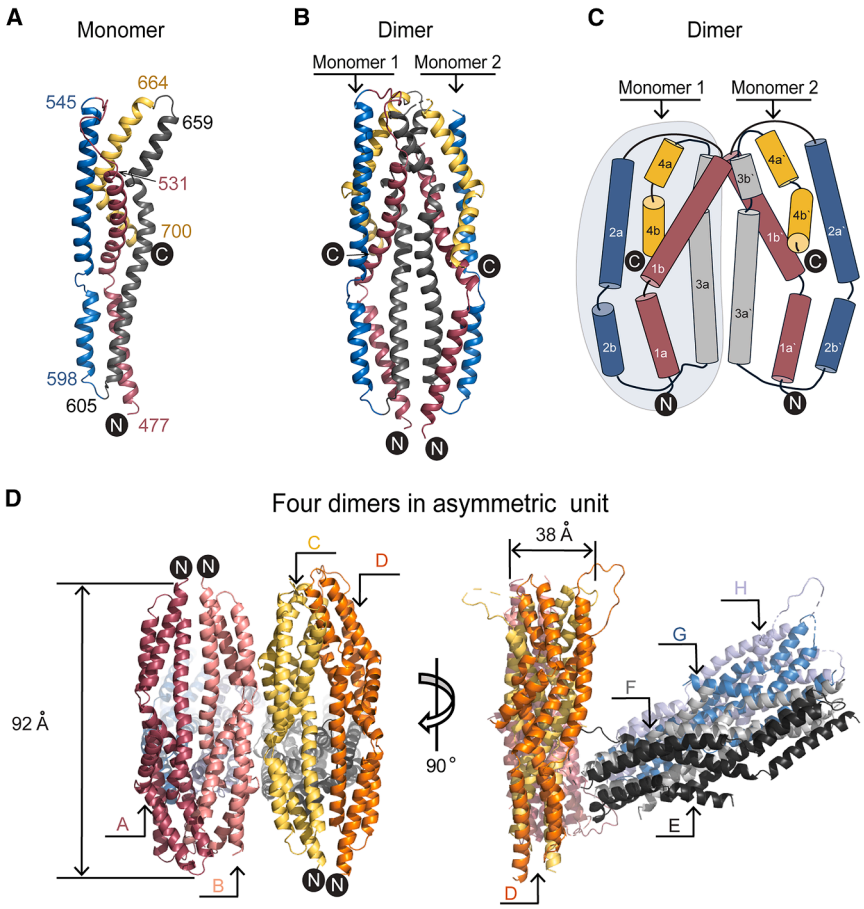

Figure 4. Crystal structure of the *Ca*Kip3 proximal tail

(A) Cartoon representation of the crystal structure of a monomer of the *Ca*Kip3 proximal tail, with individual alpha-helices color-coded: helix 1 (raspberry red; residues 477–531), helix 2 (blue; residues 545–598), helix 3 (gray; residues 605–659), and helix 4 (yellow; residues 664–700). The N and C termini are labeled.

(B) Cartoon representation of the crystal structure of a *Ca*Kip3 PT dimer (dimer AB).

(C) Topology model of the *Ca*Kip3 PT dimer, where alpha-helices are shown as colored cylinders and connecting loops as thin lines. Numbers with apostrophes indicate the helices of the second monomer (B). The dimerization interface is formed by helices 1b, 3a, and 3b.

(D) Orientation of the four dimers in the asymmetric unit of the crystal. Dimer 1 consists of monomer A (raspberry red) and B (deep salmon red). Dimer 2 consists of monomer C (yellow) and D (orange). Dimer 3 consists of monomer E (black) and F (gray). Dimer 4 consists of monomer G (sky blue) and H (light blue). Cartoon representations were generated using PyMOL.[22]

interactions, modeled as salt bridges, contribute to interface stability, including Arg515–Asp635, Lys516–Asp635, and Arg620–Glu621 (Figure 5D).

The AlphaFold3-predicted dimer of *S. cerevisiae* Kip3 exhibits a remarkably similar interface architecture, with analogous polar contacts between helices 3a and 1b' (Figure S9A). For example, **Asn628** is predicted to symmetrically engage another **Asn628** on helix 3a′, while **Arg527 and Glu639** mirror the interactions observed in *Ca*Kip3. Similarly, the heterodimeric AlphaFold3 model of the *S. pombe* Klp5/6 proximal tail reveals conserved interactions in equivalent regions (Figure S9B). Notably, mutations that disrupt these contacts, such as E575P in Klp5 or E569P in Klp6, lead to loss of kinesin-8 function and prominent spindle defects, including elongated spindles and protrusions in *S. pombe* cells.[33] AlphaFold3 models of metazoan kinesin-8 proximal tail contain several dimer-stabilizing polar and salt bridge interactions between helices 1 and 3 as well; however, the abundance, identity, and position of these residues in the proximal tail differs from their fungal counterparts and between different metazoan kinesin-8s. These findings highlight the evolutionary conservation, and suggest a functional importance, of the polar interactions that stabilize the proximal tail dimer of fungal kinesin-8s.

To directly test whether electrostatic interactions are essential for *Ca*Kip3 proximal tail dimer formation, we performed SEC-MALS of the MBP-PT construct under low- and high-salt conditions (137 mM vs. 500 mM NaCl). The MBP-PT construct eluted as a single peak with nearly identical profiles under both conditions (Figure 5E), and MALS analysis confirmed molecular masses of 133 and 129 kDa, respectively, consistent with a stable dimer. These results indicate that ionic strength has minimal effect on dimerization, supporting the conclusion that hydrophobic interactions play the dominant role in stabilizing the *Ca*Kip3 proximal tail dimer, while electrostatic interactions likely contribute to interface specificity and alignment.

Intramolecular contacts in the folded CaKip3 proximal tail monomer

Structural analysis of the *Ca*Kip3 proximal tail monomer using the ProteinTools web server[34] revealed that the four-helix bundle is stabilized a combination of electrostatic and hydrophobic interactions (Figures 6A and 6B). Specifically, three salt bridges were identified: two located within the upper lobule and one in the lower lobule. Notably, the salt bridge between Arg532 and Glu559 in *Ca*Kip3 is formed at the same site as the interaction between Arg562 and Glu545 in the AlphaFold3 model of the *S. cerevisiae* Kip3 proximal tail, suggesting evolutionary conservation of this electrostatic feature (Figure 6A).

Hydrophobic interactions are distributed along helices 1, 2, and 3 and contribute substantially to monomer stabilization. A comparison with the *S. cerevisiae* Kip3 model shows a strikingly similar hydrophobic residue pattern (Figure 6B). In the lower lobule, residues Leu582, Leu586, Ile615, Leu491, and Leu487 in *Ca*Kip3 align with Leu585, Ile589, Leu619, Val500, and Ile496 in *Sc*Kip3, respectively. Similarly, the upper lobule contains conserved hydrophobic positions, with *Ca*Kip3 residues Leu679, Ile511, Leu518, and Leu572 corresponding to *Sc*Kip3's Ile669, Ile523, Leu530, and Leu575. This high degree of

Please cite this article in press as: Trofimova et al., Fungal kinesin-8 motors dimerize by folding their proximal tail domain into a compact helical bundle, Structure (2025), https://doi.org/10.1016/j.str.2025.08.011

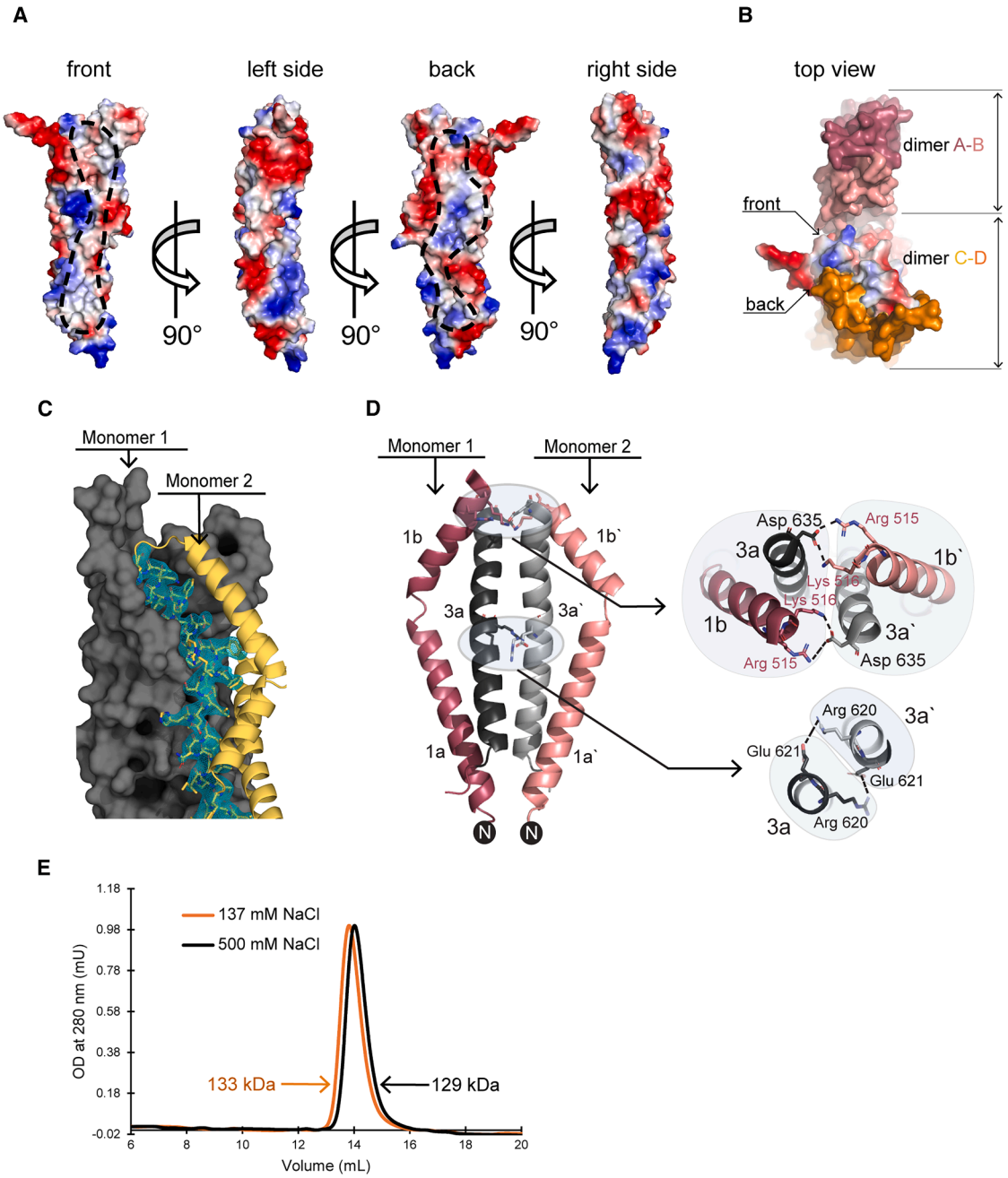

Figure 5. Structural and biochemical analysis of the *Ca*Kip3 proximal tail dimer interface

(A) Electrostatic surface representation of the *Ca*Kip3 proximal tail showing positively and negatively charged regions in blue and red, respectively, were generated using PyMOL.[22] Nonpolar regions on the front and back surfaces of a monomer that mediate intradimer (front) and interdimer (back) binding are circled with dashed lines.

(B) Top view of the intradimer and interdimer contacts observed in the *Ca*Kip3 PT crystal structure. One dimer consists of chains A and B, and the other of chains C and D.

(C) $F_{obs} - F_{calc}$ omit map of helix 3a (contoured at 3.0 σ, green-blue mesh), calculated after omitting the helix from the final model. Monomer 1 is shown as a gray surface and Monomer 2 as a yellow cartoon.

(D) Cartoon representation of the dimerization interface helices. Helices 1b and 3a interact with 1b′ and 3′a at the upper region of the bundle. Salt bridges are indicated by dashed lines.

(E) SEC-MALS profiles of the *Ca*Kip3 MBP-PT protein in low (137 mM NaCl, orange line) and high (500 mM NaCl, black line) ionic strength HEPES buffer.

Please cite this article in press as: Trofimova et al., Fungal kinesin-8 motors dimerize by folding their proximal tail domain into a compact helical bundle, Structure (2025), https://doi.org/10.1016/j.str.2025.08.011

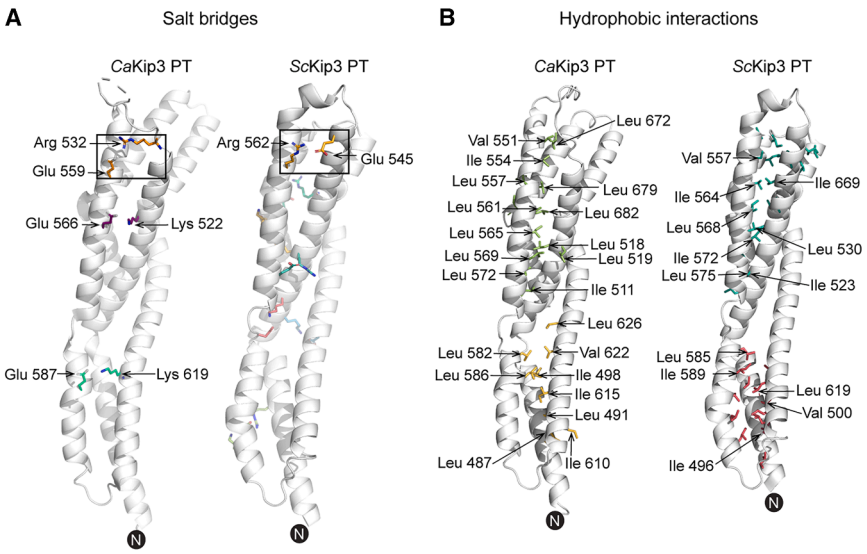

Figure 6. Intramolecular interactions stabilizing the *Ca*Kip3 and *Sc*Kip3 proximal tail monomer fold

(A) Salt bridges stabilizing the monomeric fold of *Ca*Kip3 and *Sc*Kip3 proximal tail domains are shown as colored sticks, with amino acid numbers labeled. Salt bridges at equivalent positions in *Ca*Kip3 and *Sc*Kip3 are highlighted in the box.

(B) Hydrophobic interactions within the monomers of *Ca*Kip3 and *Sc*Kip3 are depicted as sticks, with lower and upper hydrophobic clusters colored differently. *Sc*Kip3 amino acids corresponding to similar positions in *Ca*Kip3 are labeled. The N terminus of each monomer is indicated. Identification of salt bridges and hydrophobic clusters was performed using the ProteinTools application.[34]

structural and sequence conservation strongly suggests that intramolecular stabilization mechanisms are preserved among fungal kinesin-8 homologs.

Flexibility of the CaKip3 proximal tail

Although the structure is clearly stabilized by salt bridges and hydrophobic packing, analysis of the eight crystallographically unique *Ca*Kip3 proximal tail subunits revealed conformational heterogeneity. Superposition of Cα atoms from the eight subunits (A–H) yielded RMSD values ranging from 0.356 to 1.749 Å, largely due to shifts in loop regions and variations in interhelical angles. To further explore this plasticity, we employed PyMOL's Morph function to interpolate transitions between the most divergent subunits in the crystal. These morphs revealed a hinge-like region that allows relative movement between the upper and lower lobules of the four-helix bundle (Figure 7). The flexible hinge comprises the linker segments between helices 1a–1b, 2a–2b, as well as a bend in the middle of helix 3a (Figures S2 and S4). This hinge permits displacements of up to 9.4 Å for helix 1a, 8.2 Å for helix 2b, and 7.3 Å for helix 3a, suggesting the potential for dynamic remodeling of the proximal tail bundle. These conformational shifts produce structural changes on the surface of the proximal tail dimer that may modulate accessibility for regulatory interactions or binding to other components within the kinesin complex.

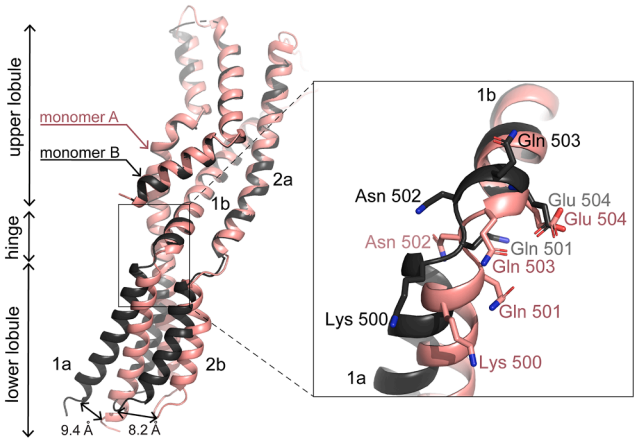

Figure 7. Bending of *Ca*Kip3 proximal tail subunits

Monomers A (deep salmon red) and B (black) were aligned via helix 1b using the Superposition/Alignment function in PyMOL.[22] Displacement of the bottom portion of helix 1a (measured at the α-carbon of Asp 478) and helix 2b (measured at the α-carbon of Asp 599) was quantified for both monomers. The inset highlights the hinge region between helix 1a and 1b, where divergence in their relative positions begins. Amino acids exhibiting the greatest variation in orientation are shown in stick representation.

The proximal tail is not directly involved in microtubule interactions

Kinesin-8 tail domains have been linked to enhanced processivity, microtubule plus-end targeting, and microtubule stabilization.[35–37] In both *S. cerevisiae* Kip3 and human Kif18A, extended regions of their tail (residues 481–805 and 802–898, respectively) have been implicated in microtubule binding,[20,37] although the specific binding motifs within these segments remain poorly defined.

To determine whether the *Ca*Kip3 proximal or distal tail contributes to microtubule interactions, we performed microtubule co-sedimentation assays using purified *Ca*Kip3 MBP-NE-PT, MBP-PT, and MBP-DT constructs (Figure 8). Each construct was incubated with increasing concentrations of taxol-stabilized microtubules, followed by ultracentrifugation to partition microtubule-bound protein (pellet) from unbound (supernatant) fractions. SDS-PAGE analysis revealed that both MBP-PT and MBP-NE-PT were present in the pellet in small amounts, but their levels did not increase with microtubule concentration (Figures 8A–8D). This lack of concentration-dependent binding indicates that their interaction with microtubules is non-specific or incidental. In contrast, the MBP-DT construct showed a robust, concentration-dependent increase in co-sedimentation with microtubules (Figures 8E and 8F), consistent with the presence of a functional microtubule-binding site in the distal tail. As expected, the construct comprising the motor domain and neck

Please cite this article in press as: Trofimova et al., Fungal kinesin-8 motors dimerize by folding their proximal tail domain into a compact helical bundle, Structure (2025), https://doi.org/10.1016/j.str.2025.08.011

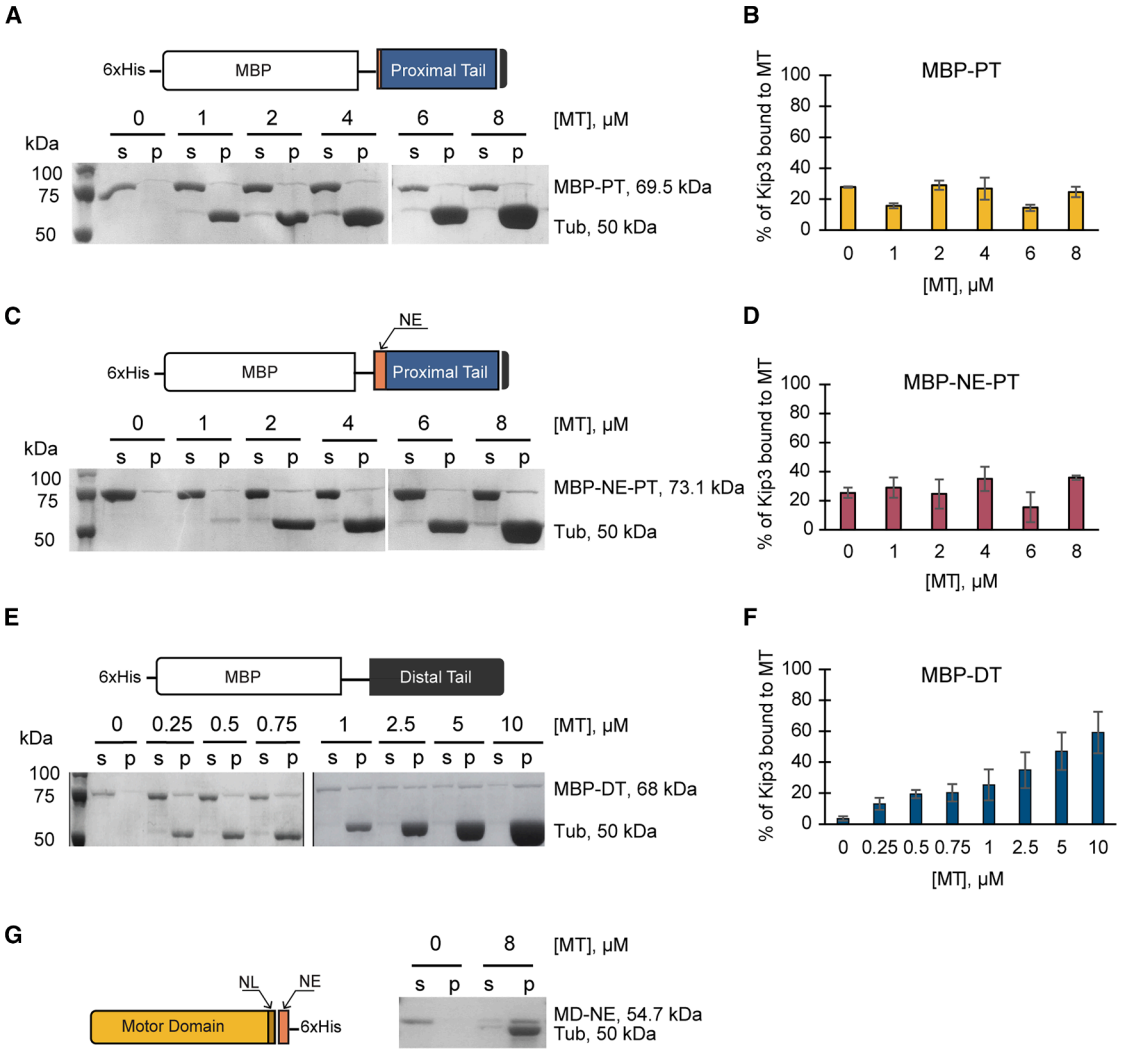

Figure 8. Microtubule binding properties of the motor domain, and proximal and distal tail regions

Representative 8% SDS-PAGE gels of the microtubule binding assay for the MBP-PT (A), MBP-NE-PT (C), MBP-DT (E), and MD-NE (G) constructs. Uncropped versions of the gels are shown in Figure S10. Kinesin proteins (1 μM) were incubated with 2 mM AMP-PNP and various concentrations of taxol-stabilized microtubules (0–10 μM, based on tubulin dimer concentration) in BRB80 buffer containing 100 mM KCl for 20 min. Binding reactions were separated by centrifugation into supernatant (S) and pellet (P) fractions for each condition. Fractions were resuspended and boiled in Laemmli buffer. Equal portions were loaded and analyzed on Coomassie brilliant blue-stained SDS-PAGE gels. Samples from separate gels are shown as non-consecutive lanes separated by a space. The percentage of microtubule-bound MBP-PT (B), MBP-NE-PT (D), and MBP-DT (F) was quantified by analyzing these gels using ImageJ software and plotted relative to the microtubule concentration. All co-sedimentation experiments were repeated three times. Data are represented as mean ± SD.

extension (MD-NE) also co-sedimented with microtubules (Figure 8G). These results demonstrate that the *Ca*Kip3 proximal tail, either alone or in combination with the neck extension, lacks microtubule-binding activity. Instead, microtubule interaction is mediated by the motor domain and distal tail regions.

DISCUSSION

This study provides a structural and functional dissection of the tail region of the *Candida albicans* kinesin-8 motor, *Ca*Kip3. We show that the *Ca*Kip3 proximal tail domain folds into a compact, four-helix bundle that dimerizes through a conserved, extensive interface within the structured proximal tail itself. Notably, this interaction does not require the adjacent neck extension region, despite its predicted coiled coil character.

These findings reveal an architectural distinction in fungal kinesin-8 motors: a robust dimerization module located ~60 Å **from the C terminus of** the motor domain, connected via an elongated, flexible neck extension. We propose that this spatial separation supports the functional versatility of kinesin-8s by allowing greater conformational freedom between motor heads. The weak or absent coiled-coil character of the neck extension may facilitate inter-protofilament switching during motility, enabling the motor to sidestep obstacles encountered along the microtubule lattice.[38–40] This ability has been described for

Please cite this article in press as: Trofimova et al., Fungal kinesin-8 motors dimerize by folding their proximal tail domain into a compact helical bundle, Structure (2025), https://doi.org/10.1016/j.str.2025.08.011

human Kif18A, as a result of demonstrating that an extended neck-linker enhanced obstacle circumvention.[40]

During microtubule depolymerization, neck extension flexibility may also enable both motor heads to simultaneously engage a curved protofilament, forming a depolymerization-competent conformation. Such an arrangement would be sterically hindered in kinesins with a short, rigid coiled-coil near the motor, as the rearward strain on the neck-linker can prevent closure of the nucleotide pocket in the leading head.[41,42] Consistent with this model, replacement of the **neck extension** in *S. cerevisiae* Kip3 with a leucine zipper significantly impairs depolymerization activity,[27] while inserting a flexible glycine linker restores function.[28] In *C. albicans* Kip3, the neck extension flexibility may also facilitate contacts between motor heads via their elongated loop-1, a feature shown to enhance depolymerase activity.[23]

Analysis of the eight unique *Ca*Kip3 PT subunits in the crystal lattice revealed a conserved four-helix bundle composed of rigid upper and lower lobules connected by a flexible hinge. Morphing between the most divergent subunits identified concerted helix motions that modulate the curvature of the proximal tail dimer surface. Although the functional role of this hinge remains speculative, its ability to reconfigure dimer shape may facilitate interactions with regulatory proteins or motor subdomains, potentially mediating allosteric signaling that tunes motor activity. Similar structural adaptability is increasingly being recognized in non-motor domains of kinesins, dyneins, and myosins, which often serve as regulatory scaffolds rather than passive linkers to cargos.[43–47] In some cases, these regions can shift from compact to extended conformations upon cofactor binding or post-translational modification, influencing motor activity or cargo engagement.[48–50]

If the proximal tail provides a platform for interaction with other molecules, our results suggest that microtubules are not among its direct binding partners. Microtubule co-sedimentation assays showed that neither the MBP-PT nor MBP-NE-PT constructs bound microtubules in a concentration-dependent manner, indicating the absence of specific, high-affinity interactions. In contrast, the distal tail construct (MBP-DT) exhibited robust microtubule binding, consistent with prior reports identifying the distal tail as the primary site for microtubule engagement.[20] These results support a model in which the proximal tail domain serves a predominantly structural role and possibly a regulatory function, stabilizing the motor dimer and enabling flexible coupling, rather than directly mediating microtubule interactions.

Altogether, our findings highlight the unique structural modularity of fungal kinesin-8s. The proximal tail functions as a compact dimerization hub, while the neck extension acts as a flexible, non-coiled mechanical linker between the dimer core and motor domains. These features distinguish kinesin-8s from other kinesin families and likely underpin their unique ability to coordinate motility and microtubule depolymerization. Future work should focus on identifying regulatory partners or modifications targeting the proximal tail, as well as conducting structure-function studies on mutant constructs that disrupt proximal tail folding. These efforts will be critical for elucidating how this domain governs the activity and regulation of fungal kinesin-8 motors.

RESOURCE AVAILABILITY

Lead contact

Requests for further information and resources and reagents should be directed to and will be fulfilled by the lead contact, John S. Allingham (allinghj@queensu.ca).

Materials availability

This study did not generate new unique reagents.

Data and code availability

- All data needed to evaluate the findings presented in the manuscript are available in the main text or the supplemental information. The X-ray crystallographic map and atomic model of the *Ca*Kip3 Proximal Tail are available in the Protein DataBank via accession code 9CRW.
- This paper does not report original code.
- Any additional information required to reanalyze the data reported in this paper is available from the lead contact upon request.

ACKNOWLEDGMENTS

This work was supported by a CIHR Project Scheme grant (PJT-169149) and an NSERC Discovery Grant (RGPIN-2019-05924). B.H. received support from the NSERC Canada Graduate Scholarships and the Ontario Graduate Scholarship programs. We thank the Canadian Light Source for beamtime and technical assistance.

AUTHOR CONTRIBUTIONS

D.T., C.D., B.H., J.D.S.A., E.D., and E.W. performed the sequence and structural analyses of kinesins using AlphaFold3 and other bioinformatic tools. B.H., C.D., and D.T. cloned, expressed, and purified the *Ca*Kip3 constructs. D.T., E.D., and J.S.A. conducted the X-ray diffraction experiments and solved the PT structure. D.T., J.D.S.A., and E.D. performed the SEC-MALS analyses. C.D. and K.M. performed that AUC analyses. D.T., C.D., and E.D. performed the biochemical assays. D.T., B.H., C.D., E.D., and J.S.A. wrote the manuscript. J.S.A. supervised the project.

DECLARATION OF INTERESTS

The authors declare no competing interests.

DECLARATION OF GENERATIVE AI AND AI-ASSISTED TECHNOLOGIES IN THE WRITING PROCESS

During the preparation of this work, the authors used Grammarly and ChatGPT to enhance clarity, streamline sentence structure, and ensure consistency of tense and terminology. After using these tools, the authors reviewed and edited the content as needed and take full responsibility for the content of the publication.

STAR★METHODS

Detailed methods are provided in the online version of this paper and include the following:

- KEY RESOURCES TABLE
- EXPERIMENTAL MODEL AND STUDY PARTICIPANT DETAILS
- METHOD DETAILS
  - Sequence analysis and structure prediction
  - Cloning, expression, and purification of proteins
  - Crystallization, data collection, and structure determination
  - Size-exclusion chromatography coupled with multi-angle light scattering (SEC-MALS)
  - Analytical ultracentrifugation (AUC)
  - Microtubule co-sedimentation assay
  - SDS-PAGE and western blot analysis
  - Quantification and statistical analysis

SUPPLEMENTAL INFORMATION

Supplemental information can be found online at https://doi.org/10.1016/j.str.2025.08.011.

Received: January 10, 2025
Revised: June 17, 2025
Accepted: August 8, 2025

REFERENCES

1. Kato, Y., Miyakawa, T., and Tanokura, M. (2018). Overview of the mechanism of cytoskeletal motors based on structure. Biophys. Rev. *10*, 571–581. https://doi.org/10.1007/s12551-017-0368-1.
2. Lan, G., and Sun, S.X. (2005). Dynamics of myosin-driven skeletal muscle contraction: I. Steady-state force generation. Biophys. J. *88*, 4107–4117. https://doi.org/10.1529/biophysj.104.056846.
3. Cooke, R. (1986). The Mechanism of Muscle-Contraction. CRC Crit. Rev. Biochem. *21*, 53–118. https://doi.org/10.3109/10409238609113609.
4. Hirokawa, N., Noda, Y., Tanaka, Y., and Niwa, S. (2009). Kinesin superfamily motor proteins and intracellular transport. Nat. Rev. Mol. Cell Biol. *10*, 682–696. https://doi.org/10.1038/nrm2774.
5. Gyoeva, F.K., Sarkisov, D.V., Khodjakov, A.L., and Minin, A.A. (2004). The tetrameric molecule of conventional kinesin contains identical light chains. Biochemistry *43*, 13525–13531. https://doi.org/10.1021/bi049288l.
6. Kanai, Y., Okada, Y., Tanaka, Y., Harada, A., Terada, S., and Hirokawa, N. (2000). KIF5C, a novel neuronal kinesin enriched in motor neurons. J. Neurosci. *20*, 6374–6384. https://doi.org/10.1523/Jneurosci.20-17-06374.2000.
7. King, S.M. (2021). Cytoplasmic factories for axonemal dynein assembly. J. Cell Sci. *134*, jcs258626. https://doi.org/10.1242/jcs.258626.
8. Paschal, B.M., King, S.M., Moss, A.G., Collins, C.A., Vallee, R.B., and Witman, G.B. (1987). Isolated flagellar outer arm dynein translocates brain microtubules in vitro. Nature *330*, 672–674. https://doi.org/10.1038/330672a0.
9. Pfister, K.K. (1999). Cytoplasmic dynein and microtubule transport in the axon: The action connection. Mol. Neurobiol. *20*, 81–91. https://doi.org/10.1007/Bf02742435.
10. Paschal, B.M., and Vallee, R.B. (1987). Retrograde transport by the microtubule-associated protein Map-1c. Nature *330*, 181–183. https://doi.org/10.1038/330181a0.
11. Sablin, E.P., Case, R.B., Dai, S.C., Hart, C.L., Ruby, A., Vale, R.D., and Fletterick, R.J. (1998). Direction determination in the minus-end-directed kinesin motor ncd. Nature *395*, 813–816. https://doi.org/10.1038/27463.
12. Kozielski, F., Sack, S., Marx, A., Thormählen, M., Schönbrunn, E., Biou, V., Thompson, A., Mandelkow, E.M., and Mandelkow, E. (1997). The crystal structure of dimeric kinesin and implications for microtubule-dependent motility. Cell *91*, 985–994. https://doi.org/10.1016/s0092-8674(00)80489-4.
13. Nithianantham, S., Iwanski, M.K., Gaska, I., Pandey, H., Bodrug, T., Inagaki, S., Major, J., Brouhard, G.J., Gheber, L., Rosenfeld, S.S., et al. (2023). The kinesin-5 tail and bipolar minifilament domains are the origin of its microtubule crosslinking and sliding activity. Mol. Biol. Cell *34*, ar111. https://doi.org/10.1091/mbc.E23-07-0287.
14. Tan, Z., Yue, Y., Leprevost, F., Haynes, S., Basrur, V., Nesvizhskii, A.I., Verhey, K.J., and Cianfrocco, M.A. (2023). Autoinhibited kinesin-1 adopts a hierarchical folding pattern. eLife *12*, RP86776. https://doi.org/10.7554/eLife.86776.
15. Locke, J., Joseph, A.P., Peña, A., Möckel, M.M., Mayer, T.U., Topf, M., and Moores, C.A. (2017). Structural basis of human kinesin-8 function and inhibition. Proc. Natl. Acad. Sci. USA *114*, E9539–E9548. https://doi.org/10.1073/pnas.1712169114.
16. Gupta, M.L., Carvalho, P., Roof, D.M., and Pellman, D. (2006). Plus end-specific depolymerase activity of Kip3, a kinesin-8 protein, explains its role in positioning the yeast mitotic spindle. Nat. Cell Biol. *8*, 913–923. https://doi.org/10.1038/ncb1457.
17. Varga, V., Helenius, J., Tanaka, K., Hyman, A.A., Tanaka, T.U., and Howard, J. (2006). Yeast kinesin-8 depolymerizes microtubules in a length-dependent manner. Nat. Cell Biol. *8*, 957–962. https://doi.org/10.1038/ncb1462.
18. Grissom, P.M., Fiedler, T., Grishchuk, E.L., Nicastro, D., West, R.R., and McIntosh, J.R. (2009). Kinesin-8 from fission yeast: a heterodimeric, plus-end-directed motor that can couple microtubule depolymerization to cargo movement. Mol. Biol. Cell *20*, 963–972. https://doi.org/10.1091/mbc.E08-09-0979.
19. Garcia, M.A., Koonrugsa, N., and Toda, T. (2002). Two kinesin-like Kin I family proteins in fission yeast regulate the establishment of metaphase and the onset of anaphase A. Curr. Biol. *12*, 610–621. https://doi.org/10.1016/S0960-9822(02)00761-3.
20. Su, X., Qiu, W., Gupta, M.L., Jr., Pereira-Leal, J.B., Reck-Peterson, S.L., and Pellman, D. (2011). Mechanisms underlying the dual-mode regulation of microtubule dynamics by Kip3/kinesin-8. Mol. Cell *43*, 751–763. https://doi.org/10.1016/j.molcel.2011.06.027.
21. Dave, S., Anderson, S.J., Sinha Roy, P., Nsamba, E.T., Bunning, A.R., Fukuda, Y., and Gupta, M.L. (2018). Discrete regions of the kinesin-8 Kip3 tail differentially mediate astral microtubule stability and spindle disassembly. Mol. Biol. Cell *29*, 1866–1877. https://doi.org/10.1091/mbc.E18-03-0199.
22. Schrodinger, LLC (2010). The PyMOL Molecular Graphics System, Version 2.3.5. http://www.pymol.org/pymol.
23. Hunter, B., Benoit, M.P.M.H., Asenjo, A.B., Doubleday, C., Trofimova, D., Frazer, C., Shoukat, I., Sosa, H., and Allingham, J.S. (2022). Kinesin-8-specific loop-2 controls the dual activities of the motor domain according to tubulin protofilament shape. Nat. Commun. *13*, 4198. https://doi.org/10.1038/s41467-022-31794-3.
24. Phillips, R.K., Peter, L.G., Gilbert, S.P., and Rayment, I. (2016). Family-specific kinesin structures reveal neck-linker length based on initiation of the coiled-coil. J. Biol. Chem. *291*, 20372–20386. https://doi.org/10.1074/jbc.M116.737577.
25. Cohen, C., and Parry, D.A. (1990). Alpha-helical coiled coils and bundles - How to design an alpha-helical protein. Proteins *7*, 1–15. https://doi.org/10.1002/prot.340070102.
26. West, R.R., Malmstrom, T., Troxell, C.L., and McIntosh, J.R. (2001). Two related kinesins, klp5+ and klp6+, foster microtubule disassembly and are required for meiosis in fission yeast. Mol. Biol. Cell *12*, 3919–3932. https://doi.org/10.1091/mbc.12.12.3919.
27. Su, X., Arellano-Santoyo, H., Portran, D., Gaillard, J., Vantard, M., Thery, M., and Pellman, D. (2013). Microtubule-sliding activity of a kinesin-8 promotes spindle assembly and spindle-length control. Nat. Cell Biol. *15*, 948–957. https://doi.org/10.1038/ncb2801.
28. Arellano-Santoyo, H., Geyer, E.A., Stokasimov, E., Chen, G.Y., Su, X., Hancock, W., Rice, L.M., and Pellman, D. (2017). A tubulin binding switch underlies Kip3/Kinesin-8 depolymerase activity. Dev. Cell *42*, 37–51.e8. https://doi.org/10.1016/j.devcel.2017.06.011.
29. Coudert, E., Gehant, S., de Castro, E., Pozzato, M., Baratin, D., Neto, T., Sigrist, C.J.A., Redaschi, N., and Bridge, A.; UniProt Consortium (2023). Annotation of biologically relevant ligands in UniProtKB using ChEBI. Bioinformatics *39*, btac793. https://doi.org/10.1093/bioinformatics/btac793.
30. Reuten, R., Nikodemus, D., Oliveira, M.B., Patel, T.R., Brachvogel, B., Breloy, I., Stetefeld, J., and Koch, M. (2016). Maltose-binding protein (MBP), a secretion-enhancing tag for mammalian protein expression systems. PLoS One *11*, e0152386. https://doi.org/10.1371/journal.pone.0152386.
31. Krissinel, E., and Henrick, K. (2007). Inference of macromolecular assemblies from crystalline state. J. Mol. Biol. *372*, 774–797. https://doi.org/10.1016/j.jmb.2007.05.022.

32. Kayikci, M., Venkatakrishnan, A.J., Scott-Brown, J., Ravarani, C.N.J., Flock, T., and Babu, M.M. (2018). Visualization and analysis of non-covalent contacts using the Protein Contacts Atlas. Nat. Struct. Mol. Biol. *25*, 185–194. https://doi.org/10.1038/s41594-017-0019-z.

33. Pinder, C., Matsuo, Y., Maurer, S.P., and Toda, T. (2019). Kinesin-8 and Dis1/TOG collaborate to limit spindle elongation from prophase to anaphase A for proper chromosome segregation in fission yeast. J. Cell Sci. *132*, 232306. https://doi.org/10.1242/jcs.232306.

34. Ferruz, N., Schmidt, S., and Höcker, B. (2021). ProteinTools: a toolkit to analyze protein structures. Nucleic Acids Res. *49*, W559–W566. https://doi.org/10.1093/nar/gkab375.

35. Stumpff, J., Du, Y., English, C.A., Maliga, Z., Wagenbach, M., Asbury, C.L., Wordeman, L., and Ohi, R. (2011). A tethering mechanism controls the processivity and kinetochore-microtubule plus-end enrichment of the kinesin-8 Kif18A. Mol. Cell *43*, 764–775. https://doi.org/10.1016/j.molcel.2011.07.022.

36. Stout, J.R., Yount, A.L., Powers, J.A., LeBlanc, C., Ems-McClung, S.C., and Walczak, C.E. (2011). Kif18B interacts with EB1 and controls astral microtubule length during mitosis. Mol. Biol. Cell *22*, 3070–3080. https://doi.org/10.1091/mbc.E11-04-0363.

37. Weaver, L.N., Ems-McClung, S.C., Stout, J.R., LeBlanc, C., Shaw, S.L., Gardner, M.K., and Walczak, C.E. (2011). Kif18A uses a microtubule binding site in the tail for plus-end localization and spindle length regulation. Curr. Biol. *21*, 1500–1506. https://doi.org/10.1016/j.cub.2011.08.005.

38. Bormuth, V., Nitzsche, B., Ruhnow, F., Mitra, A., Storch, M., Rammner, B., Howard, J., and Diez, S. (2012). The highly processive kinesin-8, Kip3, switches microtubule protofilaments with a bias toward the left. Biophys. J. *103*, L04–L06. https://doi.org/10.1016/j.bpj.2012.05.024.

39. Bugiel, M., Böhl, E., and Schäffer, E. (2015). The kinesin-8 Kip3 switches protofilaments in a sideward random walk asymmetrically biased by force. Biophys. J. *108*, 2019–2027. https://doi.org/10.1016/j.bpj.2015.03.022.

40. Malaby, H.L., Lessard, D.V., Berger, C.L., and Stumpff, J. (2019). KIF18A's neck linker permits navigation of microtubule-bound obstacles within the mitotic spindle. Life Sci. Alliance *2*, e201800169. https://doi.org/10.26508/lsa.201800169.

41. Benoit, M.P.M.H., Asenjo, A.B., Paydar, M., Dhakal, S., Kwok, B.H., and Sosa, H. (2021). Structural basis of mechano-chemical coupling by the mitotic kinesin KIF14. Nat. Commun. *12*, 3637. https://doi.org/10.1038/s41467-021-23581-3.

42. Niitani, Y., Matsuzaki, K., Jonsson, E., Vale, R.D., and Tomishige, M. (2025). Kinetic regulation of kinesin's two motor domains coordinates its stepping along microtubules. eLife *14*, RP106228. https://doi.org/10.7554/eLife.106228.2.

43. Rank, K.C., and Rayment, I. (2013). Functional asymmetry in kinesin and dynein dimers. Biol. Cell *105*, 1–13. https://doi.org/10.1111/boc.201200044.

44. Coy, D.L., Hancock, W.O., Wagenbach, M., and Howard, J. (1999). Kinesin's tail domain is an inhibitory regulator of the motor domain. Nat. Cell Biol. *1*, 288–292. https://doi.org/10.1038/13001.

45. Dietrich, K.A., Sindelar, C.V., Brewer, P.D., Downing, K.H., Cremo, C.R., and Rice, S.E. (2008). The kinesin-1 motor protein is regulated by a direct interaction of its head and tail. Proc. Natl. Acad. Sci. USA *105*, 8938–8943. https://doi.org/10.1073/pnas.0803575105.

46. Li, X.D., Jung, H.S., Wang, Q., Ikebe, R., Craig, R., and Ikebe, M. (2008). The globular tail domain puts on the brake to stop the ATPase cycle of myosin Va. Proc. Natl. Acad. Sci. USA *105*, 1140–1145. https://doi.org/10.1073/pnas.0709741105.

47. Carter, A.P., Garbarino, J.E., Wilson-Kubalek, E.M., Shipley, W.E., Cho, C., Milligan, R.A., Vale, R.D., and Gibbons, I.R. (2008). Structure and functional role of dynein's microtubule-binding domain. Science *322*, 1691–1695. https://doi.org/10.1126/science.1164424.

48. Fan, X., and McKenney, R.J. (2023). Control of motor landing and processivity by the CAP-Gly domain in the KIF13B tail. Nat. Commun. *14*, 4715. https://doi.org/10.1038/s41467-023-40425-4.

49. Kaan, H.Y.K., Hackney, D.D., and Kozielski, F. (2011). The structure of the kinesin-1 motor-tail complex reveals the mechanism of autoinhibition. Science *333*, 883–885. https://doi.org/10.1126/science.1204824.

50. Siddiqui, N., Zwetsloot, A.J., Bachmann, A., Roth, D., Hussain, H., Brandt, J., Kaverina, I., and Straube, A. (2019). PTPN21 and Hook3 relieve KIF1C autoinhibition and activate intracellular transport. Nat. Commun. *10*, 2693. https://doi.org/10.1038/s41467-019-10644-9.

51. Abramson, J., Adler, J., Dunger, J., Evans, R., Green, T., Pritzel, A., Ronneberger, O., Willmore, L., Ballard, A.J., Bambrick, J., et al. (2024). Accurate structure prediction of biomolecular interactions with AlphaFold 3. Nature *630*, 493–500. https://doi.org/10.1038/s41586-024-07487-w.

52. Elfmann, C., and Stülke, J. (2023). PAE viewer: a webserver for the interactive visualization of the predicted aligned error for multimer structure predictions and crosslinks. Nucleic Acids Res. *51*, W404–W410. https://doi.org/10.1093/nar/gkad350.

53. Vagin, A., and Teplyakov, A. (2000). An approach to multi-copy search in molecular replacement. Acta Crystallogr. D Biol. Crystallogr. *56*, 1622–1624. https://doi.org/10.1107/S0907444900013780.

54. Murshudov, G.N., Vagin, A.A., and Dodson, E.J. (1997). Refinement of macromolecular structures by the maximum-likelihood method. Acta Crystallogr. D Biol. Crystallogr. *53*, 240–255. https://doi.org/10.1107/S0907444996012255.

55. Adams, P.D., Afonine, P.V., Bunkóczi, G., Chen, V.B., Davis, I.W., Echols, N., Headd, J.J., Hung, L.W., Kapral, G.J., Grosse-Kunstleve, R.W., et al. (2010). PHENIX: a comprehensive Python-based system for macromolecular structure solution. Acta Crystallogr. D Biol. Crystallogr. *66*, 213–221. https://doi.org/10.1107/S0907444909052925.

56. Emsley, P., and Cowtan, K. (2004). Coot: model-building tools for molecular graphics. Acta Crystallogr. D Biol. Crystallogr. *60*, 2126–2132. https://doi.org/10.1107/S0907444904019158.

57. Schindelin, J., Arganda-Carreras, I., Frise, E., Kaynig, V., Longair, M., Pietzsch, T., Preibisch, S., Rueden, C., Saalfeld, S., Schmid, B., et al. (2012). Fiji: an open-source platform for biological-image analysis. Nat. Methods *9*, 676–682. https://doi.org/10.1038/nmeth.2019.

58. Schuck, P. (2000). Size-distribution analysis of macromolecules by sedimentation velocity ultracentrifugation and Lamm equation modeling. Biophys. J. *78*, 1606–1619. https://doi.org/10.1016/S0006-3495(00)76713-0.

59. Neville, N., Lehotsky, K., Yang, Z., Klupt, K.A., Denoncourt, A., Downey, M., and Jia, Z. (2023). Modification of histidine repeat proteins by inorganic polyphosphate. Cell Rep. *42*, 113082. https://doi.org/10.1016/j.celrep.2023.113082.

Please cite this article in press as: Trofimova et al., Fungal kinesin-8 motors dimerize by folding their proximal tail domain into a compact helical bundle, Structure (2025), https://doi.org/10.1016/j.str.2025.08.011

STAR★METHODS

KEY RESOURCES TABLE

REAGENT or RESOURCE	SOURCE	IDENTIFIER
Antibodies		
anti-6×Histidine Tagged primary antibody	Millipore	Cat# 05-949; RRID: AB_492660
Anti-Mouse DyLight™ 680 secondary antibody	Invitrogen	Cat# 35518; RRID: AB_614942
Bacterial and virus strains		
E. coli BL21 (DE3)	Novagen	Cat#69450
Chemicals, peptides, and recombinant proteins		
Lysozyme	BioShop	Cat#LYS702
Isopropyl β-D-1-thiogalactopyranoside (IPTG)	Bioshop	Cat#IPT001
Compete EDTA-free protease inhibitor	Thermo scientific	Cat#A32965
HEPES (free acid)	Bioshop	Cat#HEP001
2-mercaptoethanol	Bioshop	Cat#MER002
Nickel-NTA Agarose	Thermo-Fisher	Cat#A50584
Superdex™ 200 Increase 10/300 GL	Cytiva	Cat#28990944
HiLoad 26/60 Superdex™ 200 PG	GE Healthcare	Cat#17-1071-01
polyethylene glycol (PEG) 6000	Acros organics	Cat#192280010
AMP-PNP	Sigma	Cat#A2647
ATP	Bioshop	Cat#ATP007
Taxol	Toronto Research Chemicals	Cat#P132500
Deposited data		
Atomic model of the *Candida albicans* Kip3 proximal tail	This paper	PDB: 9CRW
Oligonucleotides		
*Ca*Kip3 MD-PT_ *pET24d*(+) (forward) TGAAAGACGCGCAGACTAATTGAG ATCCGGCTGCTAACAA	This paper	N/A
*Ca*Kip3 MD-PT_ *pET24d*(+) (reverse) TTACCTTCTTCGATTTTCATATGGTG GTGATGATGGTGTT	This paper	N/A
*Ca*Kip3 MBP-NE-PT_*HT29* (forward) TAATTCGCCGTCCGGCGGCGCTGC CGCTCATGTTGGTTCCTATCTGAA	This paper	N/A
*Ca*Kip3 MBP-NE-PT_*HT29* (reverse) AGTCACGATGCGGCCGCTCGAGTT ATTCTGATTCAACTTTATTCT	This paper	N/A
*Ca*Kip3 MBP-PT_*HT29* (forward) TTCGCCGTCCGGCGGCGCTGCCG CTAACAAACGCAAAGACCTGGA	This paper	N/A
*Ca*Kip3 MBP-DT_*HT29* (forward) ATTTACGTAAGGATCCAATCCGGAT GAAAGTATGATGTCTATA	This paper	N/A
*Ca*Kip3 MBP-DT_*HT29* (reverse) GTCATGATCTCTCGAGTTAATTATC GTTGCTAATTTTGCTTGC	This paper	N/A
HT29_vector backbone (forward) CTCGAGCGGCCGCATCGTGACTG ACTGAGATCCGGCTGCTAA	This paper	N/A

(*Continued on next page*)

Please cite this article in press as: Trofimova et al., Fungal kinesin-8 motors dimerize by folding their proximal tail domain into a compact helical bundle, Structure (2025), https://doi.org/10.1016/j.str.2025.08.011

Continued

REAGENT or RESOURCE	SOURCE	IDENTIFIER
HT29_vector backbone (reverse) AGCGGCAGCGCCGCCGGACGGC GAATTAGTCTGCGCGTC	This paper	N/A
Recombinant DNA		
*Ca*Kip3 MD-NL_ *pET24d*(+)	Hunter et al.[23]	N/A
*Ca*Kip3 MD-NE_ *pET24d*(+)	Hunter et al.[23]	N/A
*Ca*Kip3 MD-PT_ *pET24d*(+)	This paper	N/A
*Ca*Kip3 MBP-NE-PT_*HT29*	This paper	N/A
*Ca*Kip3 MBP-PT_*HT29*	This paper	N/A
*Ca*Kip3 MBP-DT_*HT29*	This paper	N/A
MBP_*HT29*	This paper	N/A
Software and algorithms		
UniProtKB	Coudert et al.[29]	www.uniprot.org
AlphaFold3	Abramson et al.[51]	https://alphafoldserver.com/
PyMOL	Schrodinger, LLC[22]	https://www.pymol.org/
PAE Viewer	Elfmann and Stulke[52]	https://pae-viewer.uni-goettingen.de/
PDBePISA server	Krissinel et al.[31]	https://www.ebi.ac.uk/pdbe/pisa/
Protein Contacts Atlas	Kayikci et al.[32]	http://pca.mbgroup.bio/
MXProc	Canadian Macromolecular Crystallography Facility	https://github.com/michel4j/mxproc
MolRep	Vagin and Teplyakov[53]	https://www.ccp4.ac.uk/html/molrep.html
Refmac	Murshudov et al.[54]	https://www.ccp4.ac.uk/html/refmac5.html
Phenix Refine	Adams et al.[55]	https://phenix-online.org/
Coot	Emsley and Cowtan[56]	https://www2.mrc-lmb.cam.ac.uk/personal/pemsley/coot/
ASTRA 7.1.4	Wyatt Technology	https://www.wyatt.com/products/software/astra.html
ImageJ	Schindelin et al.[57]	https://imagej.net/ij/
SEDFIT	Schuck[58]	https://sedfitsedphat.github.io/

EXPERIMENTAL MODEL AND STUDY PARTICIPANT DETAILS

Recombinant proteins were expressed in *E. coli* BL21 (DE3), incubated at 25°C. Tubulin was obtained from bovine brain.

METHOD DETAILS

Sequence analysis and structure prediction

Protein sequences for the *Ca*Kip3 (A0A1D8PKA4), *Sc*Kip3 (P53086), *Fo*Kip3 (A0A2H3TME4), *Sp*Klp5/6 (O14343/O59751), *Dm*Klp67A (P91945), *Hs*Kif18A (Q8NI77), and *Hs*Kif19 (Q2TAC6) were obtained from UniProt.[29] Dimeric structural models were generated using AlphaFold3.[51] Two Mg^{2+} ions and two ATP ligands were included in all predictions to fill the nucleotide pocket of their motor domains. Local folding accuracy was evaluated by predicted Local Distance Difference Test (pLDDT) score for each atom in the models, with the AlphaFold3 recommended score thresholds of 0, 50, 70, and 90 for Very Low, Low, High, and Very High confidence, respectively. Interdomain interaction predictions were evaluated based on the predicted aligned error (PAE) score[51] and visualized by the PAE Viewer webserver.[52] Congruence between the AlphaFold3-predicted *Ca*Kip3 proximal tail dimer and the crystal structure was performed using the Superposition/Alignment function in PyMOL.[22]

Cloning, expression, and purification of proteins

Constructs encoding *Ca*Kip3 NE-PT, PT, and DT regions were PCR-amplified from the *Kip3N972_pET24d(+)* plasmid[23] and cloned into the HT29 vector using Gibson assembly. HT29, a pET16b-derived expression vector, includes N-terminal 6xHis and maltose-binding protein (MBP) tags.[59] Constructs encoding *Ca*Kip3 MD-NL, MD-NE, and MD-PT were PCR-amplified, along with a C-terminal

Please cite this article in press as: Trofimova et al., Fungal kinesin-8 motors dimerize by folding their proximal tail domain into a compact helical bundle, Structure (2025), https://doi.org/10.1016/j.str.2025.08.011

6xHis tag, from the *Kip3N972_pET24d(+)* plasmid[23] and assembled into circular plasmids using Gibson assembly. All plasmids were sequence-verified to confirm proper assembly. The *Ca*Kip3 MD-NL and MD-NE constructs were previously generated in our laboratory.[23]

Plasmids were transformed into *E. coli* BL21 (DE3), grown in LB media supplemented with the appropriate antibiotics, and protein expression was induced with 1 mM isopropyl β-D-1-thiogalactopyranoside (IPTG) at 25°C overnight. Cell pellets were harvested by centrifugation, lysed by sonication in lysis buffer (50 mM sodium phosphate, pH 8, 500 mM NaCl, 5 mM 2-mercaptoethanol, 0.2 mg/mL lysozyme, and protease inhibitors), and clarified by centrifugation at 125,700 × g for 25 min. The lysis buffer used for cells expressing the motor domain-containing constructs (MD-NL, MD-NE, and MD-PT) was supplemented with 2 mM $MgCl_2$ and 0.2 mM ATP.

Proteins were purified by Ni-NTA affinity chromatography using PBS buffer (10 mM sodium phosphate, 300 mM NaCl, 20 mM imidazole, 5 mM 2-ME, pH 8.0), eluted with 300 mM imidazole, pooled, and dialyzed overnight into HEPES buffer (20 mM HEPES, 150 mM NaCl, 1 mM DTT, pH 7.2). Final purification was done using a Superdex 200 size-exclusion column equilibrated in HEPES buffer. Target fractions were pooled, concentrated to 20-25 mg/mL, flash-frozen, and stored at −80°C. All buffers used during the purification of the motor domain-containing constructs (MD-NL, MD-NE, and MD-PT) were supplemented with 1 mM $MgCl_2$ and 0.2 mM ATP.

Crystallization, data collection, and structure determination

Crystals grew when the *Ca*Kip3 MBP-PT protein construct was incubated in 5 μL hanging drops containing a 1:1 ratio of the protein (20 mg/mL) and a precipitant solution (0.1 M Tris pH 8.5, 18% polyethylene glycol (PEG) 6000) at 293 K over 7 days. Crystals were flash-cooled in liquid nitrogen prior to X-ray diffraction. Diffraction data were collected at beamline 08ID-1 of the Canadian Light Source (100 K) and processed using MXProc. The *Ca*Kip3 PT structure was solved by molecular replacement with the AlphaFold3-predicted model of the proximal tail monomer using MolRep.[53] Refinement was performed with Refmac[54] and Phenix Refine,[55] with manual adjustments in Coot.[56] Data processing and refinement statistics are summarized in Table 1. Coordinates and structure factors have been deposited in the Protein Data Bank (Accession Code: 9CRW).

Table 1. X-ray diffraction data collection, refinement, and validation statistics

	*Ca*Kip3 Proximal tail (PDB ID: 9CRW)
Data collection	
Wavelength	0.95299
Resolution range (Å)	47.84–2.49 (2.55–2.49)
Space group	$P2_1$
Unit-cell	
a, b, c (Å)	84.0, 104.6, 118.8
α, β, γ (°)	90.0, 93.4, 90.0
Unique reflections	140148 (2489)
Multiplicity	7.0 (2.69)
Completeness (%)	98.73 (92.82)
Average I/σ(I)	11.2 (0.8)
Wilson B-factor ($Å^2$)	66.75
^{R}merge	0.07
^{R}pim	0.028
^{R}meas	0.028
Structure refinement	
No. of reflections	139427
^{R}work	0.234
^{R}free	0.278
RMSD bond lengths (Å)	0.01
RMSD bond angles (°)	1.154
^{B}ave ($Å^2$)/protein atoms	101.0/14593
Ramachandran favored (%)	94.53
Ramachandran allowed (%)	5.24
Ramachandran outliers (%)	0.23

Statistics for the highest-resolution shell are shown in parentheses.

Please cite this article in press as: Trofimova et al., Fungal kinesin-8 motors dimerize by folding their proximal tail domain into a compact helical bundle, Structure (2025), https://doi.org/10.1016/j.str.2025.08.011

CellPress

Size-exclusion chromatography coupled with multi-angle light scattering (SEC-MALS)

Proteins (20 μM) in HEPES buffer supplemented with 1 mM $MgCl_2$ and 0.2 mM ATP were analyzed using an ÄKTA Pure FPLC system with a Superdex 200 column (Cytiva) coupled to a TREOS II light-scattering detector and an Optilab T-rEX refractive index detector (Wyatt Technology). Molecular weights were determined using ASTRA 7.1.4 software (Wyatt Technology).

Analytical ultracentrifugation (AUC)

Proteins (20 μM) in 310 μL of HEPES buffer were equilibrated at 20°C and loaded into double-sector epon-filled centerpieces with buffer in the reference compartments. Sedimentation velocity analysis was performed at 40,000 rpm using a Beckman Coulter XL-I ultracentrifuge with absorbance at 290 nm. Absorbance scans were collected every 2 min. Sedimentation boundaries were fitted to a continuous size distribution c(s) model using SEDFIT.[58]

Microtubule co-sedimentation assay

Taxol-stabilized microtubules (20 μM) obtained from bovine brain were prepared in BRB80 buffer (80 mM PIPES, 1 mM $MgCl_2$, 1 mM EGTA, 1 mM DTT, pH 6.8).[23] Pre-spun kinesin constructs (155,000 × *g*, 25 min, 25°C) were incubated with varying concentrations of microtubules (0–10 μM) in reaction buffer (2 mM AMP-PNP, 1 μM kinesin, 20 μM Taxol, 100 mM KCl) for 20 min at 25°C. Reactions were centrifuged (155,000 × *g*, 25 min), and supernatant and pellet fractions were analyzed by SDS-PAGE with Coomassie Blue staining. Band intensities were quantified using ImageJ.[57] All assays were performed in triplicate.

SDS-PAGE and western blot analysis

*Ca*Kip3 PT crystals were washed, dissolved in water, and mixed with 2× SDS loading buffer. Samples were separated by SDS-PAGE and stained with Coomassie Blue or transferred to PVDF membranes for Western blotting. Membranes were blocked in 1% milk, probed overnight at 4°C with anti-6×His primary antibody (Millipore #05-949, 1:1000), followed by secondary antibody (Anti-Mouse DyLight 680, Invitrogen #35518, 1:5000) for 1 h at room temperature. Blots were visualized on an Odyssey DLx imaging system.

Quantification and statistical analysis

Local folding accuracy of the AlphaFold3 models was evaluated by predicted Local Distance Difference Test (pLDDT) score and is reported in Figure S3A. Interdomain interaction predictions were evaluated based on the predicted aligned error (PAE) score and visualized by the PAE Viewer webserver (Figure S3B). X-ray crystallography data collection and refinement statistics are summarized in Table 1. Multi-angle Light Scattering (MALS) data was analyzed by the ASTRA 7.1.4 software (Wyatt Technology) to obtain molecular weights of the *Ca*Kip3 protein constructs. For molecular weight determination by analytical ultracentrifugation analysis, the sedimentation boundaries of the *Ca*Kip3 protein constructs were fitted to a continuous size distribution c(s) model using SEDFIT.[58] Microtubule-binding data was obtained from three replicate co-sedimentation experiments, and is expressed in Figures 8B, 8D, and 8F as mean ± SD.